Super-resolution Imaging of Structure, Molecular Composition, and Stability of Single Oligonucleotide Polyplexes

Natalia Feiner-Gracia,[†,∥,⊥] R. Alis Olea,[†,‡,⊥] Robert Fitzner,[§] Najoua El Boujnouni,[‡] Alexander H. van Asbeck,[‡] Roland Brock,[*,‡] and Lorenzo Albertazzi[*,†,∥]

[†]Nanoscopy for Nanomedicine Group, Institute for Bioengineering of Catalonia (IBEC), The Barcelona Institute of Science and Technology (BIST), Carrer Baldiri Reixac 15-21, 08024 Barcelona, Spain

[‡]Department of Biochemistry, Radboud Institute for Molecular Life Sciences, Radboud University Medical Center, Nijmegen, The Netherlands

[§]Department of Mathematics and Computer Science, Eindhoven University of Technology, Post Office Box 513, 5600 MD Eindhoven, The Netherlands

[∥]Department of Biomedical Engineering, Institute for Complex Molecular Systems (ICMS), Eindhoven University of Technology, 5612AZ Eindhoven, The Netherlands

S *Supporting Information*

ABSTRACT: The successful application of gene therapy relies on the development of safe and efficient delivery vectors. Cationic polymers such as cell-penetrating peptides (CPPs) can condense genetic material into nanoscale particles, called polyplexes, and induce cellular uptake. With respect to this point, several aspects of the nanoscale structure of polyplexes have remained elusive because of the difficulty in visualizing the molecular arrangement of the two components with nanometer resolution. This limitation has hampered the rational design of polyplexes based on direct structural information. Here, we used super-resolution imaging to study the structure and molecular composition of individual CPP-mRNA polyplexes with nanometer accuracy. We use two-color direct stochastic optical reconstruction microscopy (dSTORM) to unveil the impact of peptide stoichiometry on polyplex structure and composition and to assess their destabilization in blood serum. Our method provides information about the size and composition of individual polyplexes, allowing the study of such properties on a single polyplex basis. Furthermore, the differences in stoichiometry readily explain the differences in cellular uptake behavior. Thus, quantitative dSTORM of polyplexes is complementary to the currently used characterization techniques for understanding the determinants of polyplex activity in vitro and inside cells.

KEYWORDS: *Super-resolution microscopy, gene delivery, dSTORM, polyplexes, stability*
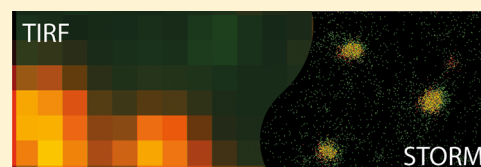
Cell-penetrating peptides (CPPs), also known as protein transduction domains, are a very promising class of vectors for gene delivery[1] because of their ability to facilitate cell entry of conjugated molecules.[2,3] Moreover, because of their positive charge, CPPs are ideal candidates for the noncovalent complexation of negatively charged oligonucleotides into nanosized particles named polyplexes.[4] The potential of polyplexes to deliver different oligonucleotide cargo such as plasmid DNA or RNA into cells for gene therapy has been widely explored.[5−7] Recently, mRNA has emerged as another promising option.[8−10] Polyplexes of mRNA only need to penetrate cells and escape from the endosomes or lysosomes to the cytoplasm, where mRNA gets translated immediately into proteins. Furthermore, mRNA is only transiently active without the risk of insertion into the host genome, and it is fully degraded via physiological mechanisms. Therefore, mRNA-loaded polyplexes have recently been proposed as efficient carriers for oligonucleotide therapy.[8−10]

Despite the many gene carriers proposed and studied, the design of the polyplexes is still very challenging, and activity varies greatly.[11] This may also be attributed to the fact that the structure space of delivery vectors has been navigated with a limited understanding of the structural properties and variations of the fabric of a polyplex. In fact, only a handful of methods for polyplex characterization are currently available. The average hydrodynamic size and charge of the polyplexes can be measured using dynamic light scattering (DLS) and zeta potential or electrophoretic shift assays, respectively.[7] Also, images from electron microscopy (EM) and atomic force microscopy (AFM) can indicate the polyplex size and shape,[12] thus providing information on morphological changes.[13,14] The efficiency of complexation is evaluated using gel electrophoresis by detecting the presence of free oligonucleotides, while the affinity is currently measured using a dye exclusion assay.[7] Overall, each of the current methods supplies valuable information; however, they exhibit two main limitations: (i)
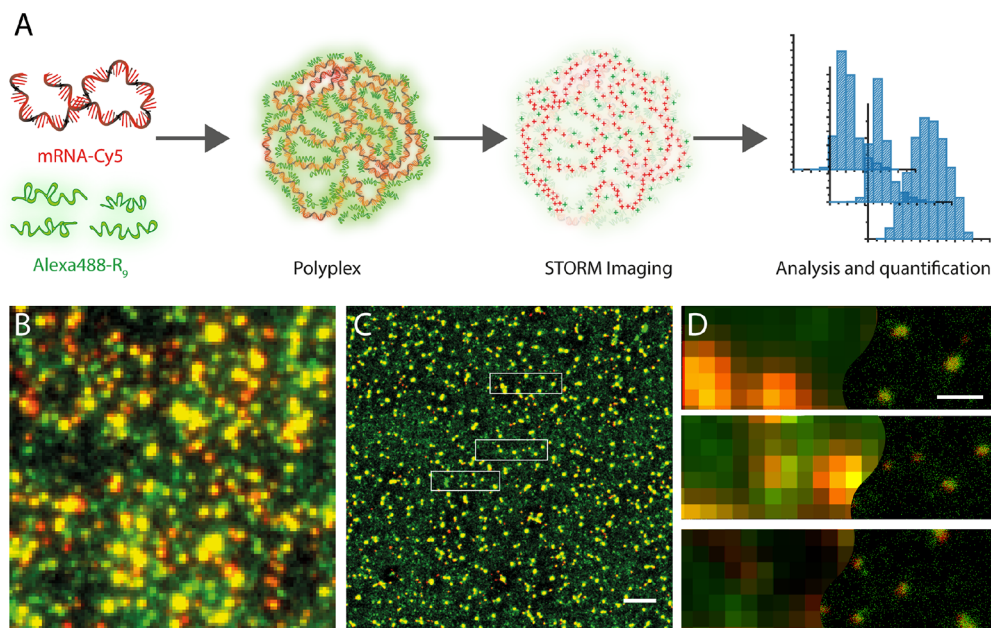
Figure 1. Imaging of polyplexes using dSTORM microscopy. (A) Schematic representation of polyplex formation from mRNA-Cy5 and AlexaFluor488-R9, with imaging and analysis. (B) Conventional fluorescent image of polyplexes at N/P 5 (red represents mRNA molecules and green R9 molecules). (C) dSTORM imaging of polyplexes, with the same field of view as in B. Scale bar 2 μm. (D) Close-up images of three different areas showing low-resolution data on the left and high-resolution data on the right. Scale bar 400 nm.

they are mostly ensemble techniques providing average information for the polyplexes and (ii) they are not able to distinguish between the two components of the polyplex and therefore miss quantitative and qualitative aspects of the composition and inner organization of individual polyplexes. Therefore, only very limited data is available for composing molecular models of the structure and the composition of polyplexes.[15−17]

Here, we propose the use of two-color direct stochastic optical reconstruction microscopy (dSTORM) to unveil the structure and composition of polyplexes on a single-particle basis. Recently, it has been demonstrated that dSTORM can be used to image synthetic nanoparticles with different chemical natures and sizes.[18−20] The nanometric resolution, down to 20 nm, provided by this technique together with the possibility to obtain two-color images is very promising for the character-ization of multicomponent nanometric assemblies such as polyplexes. With the appropriate knowledge of the photo-physical properties of the dye such as the duty cycle and bleaching rate, STORM provides the possibility to obtain quantitative information about stoichiometries and absolute molecule numbers. In this framework, membrane recep-tors,[21−23] DNA origami DNA strands,[24] and accessible binding sites on endocytic/endosomal vesicles[25] were quantified. Therefore, dSTORM can also contribute to the quantitative understanding of polyplexes. Despite this potential, to the best of our knowledge, the use of super-resolution for the study of gene delivery carriers has not been explored.

One of the most important experimental degrees of freedom in polyplex generation is the ratio of the cationic moiety and nucleic acids, which determines the N/P ratio, the ratio of positive over negative charge carriers. The N/P ratio determines several key properties of the formed polyplexes such as the net charge, size, and stability.[11,26] We considered the N/P ratio to be an ideal test case to establish a direct quantitative analysis of polyplex composition using super-resolution dSTORM micros-

copy. Gene-delivery carriers consisting of mRNA complexed with the peptide nona-arginine (R9) were imaged with molecular resolution. Owing to the ability to simultaneously measure the size and composition of polyplexes, our results show both qualitative and quantitative differences in the content of mRNA and CPPs for different N/P ratios. Moreover, dSTORM imaging can be performed in a complex matrix, which allowed us to visualize changes in polyplex structure in blood serum. This is key information becauase one of the reasons for the failure of gene carriers in vivo is the lack of stability in blood. Finally, we demonstrate that the information on polyplex stoichiometry obtained by STORM readily explains quantitative differences in the cellular uptake of the polyplexes. Our results highlight the potential of super-resolution microscopy to play a pivotal role in the study of polyplexes, complementing the existing methodologies and contributing to the rational design of new structures to enhance cell transfection.

For our dSTORM analysis, we prepared polyplexes formed by the CPP L-nona-arginine (R9) with a 1929-nucleotide-long mRNA coding for firefly luciferase. R9 is a well-known cell-penetrating peptide, and its capacity to complex and induce the cellular uptake of oligonucleotides has been previously studied.[11,27,28] An overview of our procedure is reported in Figure 1a. To perform dSTORM imaging, both components were labeled using the dSTORM-compatible, spectrally well-separated dyes, AlexaFluor488 and Cyanine 5 for R9 and mRNA, respectively. The peptide was labeled at the N-terminus. The mRNA was stochastically labeled with Cy5-UTP with an average labeling ratio of 27 dyes per molecule, as estimated from UV/vis absorption measurements (as detailed in Supporting Information). The labeling ratio (i.e,. the proportion of labeled molecules) was optimized to obtain an optimal signal density for dSTORM, as described extensively in the Materials and Methods section. STORM images of polyplexes with nonlabeled molecules were obtained as a control, showing almost no localization (Supporting Information Figure S6). After complex-
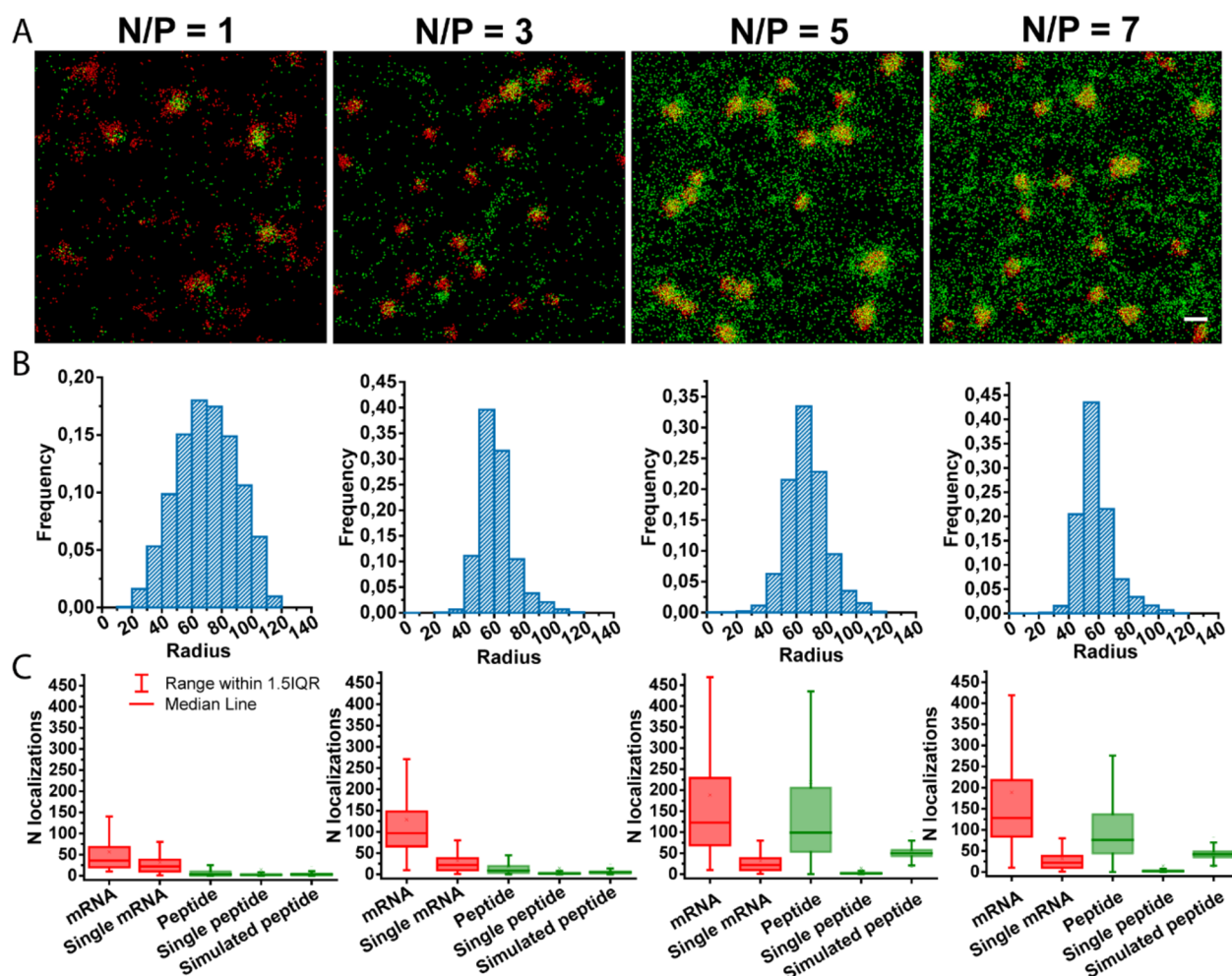
Figure 2. Structure and stoichiometry differences of polyplexes. (A) dSTORM images of polyplexes prepared at N/P ratios of 1, 3, 5, and 7 from left to right. (B) Frequency histograms of the size of the polyplexes quantified from the STROM images for each N/P ratio. (C) Box plot comparing the number of localizations of mRNA and peptide quantified for each N/P ratio together with the quantification of single molecules and the number of localizations obtained from the simulations. Statistical analyses were run (Mann−Whitney test), showing significant differences between the peptide content in NP3 and NP5 ($p < 0.0001$) and the mRNA content between NP1 and NP3 ($p < 0.0001$). Scale bar 200 nm.

ation, the polyplexes were deposited on a glass coverslip for dSTORM imaging. Figure 1B,C shows representative images of R9-mRNA polyplexes at an N/P ratio of 5. We had seen before that well-defined polyplexes were formed for N/P ratios larger than 3.

The direct comparison between conventional (B) and dSTORM (C) microscopy images shows how the improvement of resolution allows individual polyplexes to be resolved, while in the conventional image it is impossible to distinguish a single polyplex from clusters. Images revealed complexes of 50−75 nm in radius, in agreement with DLS measurements (Supporting Information Figure S7). Interestingly, a large amount of green signal (which corresponds to the peptide) was not associated with the polyplexes, indicating that not all of the peptide used in the complexation procedure was incorporated. This observation is of special interest as most of the other characterization methods (e.g., DLS, TEM, AFM, and gel electrophoresis) cannot detect individual peptides and are strongly biased toward the macromolecular assemblies. Notably, free cationic moieties may play a role in the transfection and/or toxicity. As an example, previous studies of Vaidyanathan et al. proved the enhanced pDNA endosomal escape of polyplexes due to the addition of free PEI polymer.[29] Moreover, for acylated TP10

analogs, nonincorporated peptide at higher N/P ratios showed enhanced toxicity.[30] Therefore, being able to visualize the noncomplex materials is of crucial importance.

In addition, dSTORM imaging allowed the study of the distribution of the peptide and the mRNA within the polyplexes as magnified in Figure 1D. The observed overlap of the two colors indicates that mRNA and R9 molecules are homogeneously intertwined inside the polyplex, at least within the resolution of dSTORM. A dSTORM 3D image was acquired to prove these observations and rule out the effect of the projection, and a middle stack of a polyplex in Supporting Information Figure S8 shows that both molecules are indeed intertwined. This result proves that mRNA molecules are not exposed on the polyplex surface but are shielded within the structure. This information is of utmost importance when designing effective gene delivery systems because confined mRNA will be more stable than exposed mRNA.[31]

Having successfully obtained super-resolution images of polyplexes formed at N/P 5, we further aimed to compare the structure and distribution of mRNA and R9 molecules for different N/P ratios. For this purpose, we imaged polyplexes formed at N/P 1, 3, 5, and 7. The mRNA concentration was maintained at a constant value in order to follow the

complexation of the same amount of oligonucleotides. In Figure 2A, a representative image of each condition is shown. At N/P 1, the mRNA-Cy5 signal was not clustered, resulting in more spread structures compared to the images obtained for N/P 5. Only minimal mRNA signal colocalized with the Alexa488-R9 signal and mostly free mRNA and free peptides were present, suggesting that the amount of R9 present at N/P 1 was not sufficient to condense mRNA into polyplexes. The distribution of mRNA changed dramatically at N/P 3, for which clear rounded clusters of mRNA-Cy5 were present. Therefore, we concluded that the R9 concentration present at N/P 3 was sufficient to compact the mRNA into polyplexes. The N/P 5 and N/P 7 polyplexes clearly contained more R9 than the N/P 3 ones. Both N/P 5 and N/P 7 were very similar to each other, which indicates that the charges in the mRNA were already saturated and the extra R9 remained in solution and was not incorporated into the polyplexes. Overall, this qualitative evaluation of dSTORM images of polyplexes formed at different N/P ratios provided important structural information regarding the mRNA and R9 interplay in the formation of polyplexes.

In dSTORM, the image reconstruction is based on single-molecule localizations detected during the imaging.[32] Therefore, dSTORM provides a highly powerful approach to analyzing the polyplexes not only qualitatively but also quantitatively.[33] Using an adapted version of a previously developed MatLab script,[34] the localizations in the mRNA-Cy5 channel were clustered in order to remove the free R9 localizations on the glass coverslip and to provide an estimation of the localizations of mRNA and CPP molecules at different complexation ratios. (The procedures are described in the SI.) In Figure 2B, the size of the polyplexes quantified for each N/P ratio is plotted on a frequency histogram. The radius of the polyplexes was between 60 and 80 nm under all conditions; however, the polydispersity of N/P 1 was significantly higher compared to that of the other ratios. N/P 1 polyplexes had a significant population of polyplexes exceeding 100 nm in size, indicating that under this condition most of the mRNA molecules were not packaged. For N/P 3 to 7, the formation of polyplexes reduced the size of the structures, also obtaining more monodisperse populations with no significant differences between N/P 3 and 7. Notably, for all conditions, the sizes quantified by dSTORM matched the DLS ensemble measurements (Supporting Information Figure S7).

In Figure 2C, the median number of localizations per polyplex detected for each N/P ratio, which is proportional to the number of molecules of the specific component, is plotted to unveil the composition of the polyplexes for the different conditions. More than 15 000 polyplexes were measured per N/P ratio. The frequency histogram of the number of localizations is represented in Supporting Information Figures S9−S12.

To better understand the data in Figure 2C, the median number of localizations per polyplex was plotted together with two more conditions: (i) polyplexes with only one labeled mRNA molecule or only one labeled R9 molecule and (ii) simulated data obtained from a stochastic blinking model. (See the Supporting Information for further details.) The results for polyplexes with only one labeled molecule are crucial to interpreting the data from the measured polyplexes because they provide a reference for the estimation of the number of molecules per polyplex (e.g., they distinguish single uncomplexed RNA strands from multiple RNAs in a particle). On the other hand, the simulations can unmask the stochastics of the dSTORM blinking, one of the main issues of dSTORM quantification, and provide the possibility to compare the

median number of localizations that was detected experimentally with a theoretical framework. As previously shown,[35] stochastic simulations can predict the expected number and distribution of localizations of a set number of molecules. Therefore, comparing the number of localizations per polyplex that were experimentally detected to simulated data can provide a more accurate estimation of the composition of individual polyplexes. To obtain the simulated data presented in Figure 2C, the following steps were performed: (i) we acquired dSTORM images of polyplexes with a single labeled R9 molecule from which we estimated the photophysical parameters of the AlexaFluor488 dye; (ii) we introduced these parameters together with the known experimental data such as the number of frames and the number of polyplexes to be simulated; (iii) we simulated the blinking behavior of a single R9 molecule and verified that the output number of localizations per cluster corresponded to the experimental one (detailed information on the simulation can be found in the Supporting Information); and (iv) data reported in Figure 2C was obtained by simulating the blinking behavior of a Poissonian population of polyplexes with a specific number of peptides. The distributions of simulated and experimentally detected localizations were compared to determine which simulated peptide number matched the peak of the experimental data (e.g., higher peptide numbers for high N/P ratios). Notably, for mRNA no simulation was conducted because of the heterogeneous labeling of the mRNA, which together with the stochastic nature of the detection could not be approximated.

From the experimental and simulated data presented in Figure 2C, comprehensive information on the polyplex structure and composition can be obtained. For N/P 1, the number of mRNA localizations was comparable to that for a single molecule supporting the hypothesis that single mRNA molecules were present that were not complexed into polyplexes. For N/P 3, the experimentally determined median number of mRNA localizations significantly increased to about 2 to 3 times that of the single molecule and remained stable at N/P ratios of 5 and 7. These results indicate that inside each polyplex there were only a few mRNA molecules. Interestingly, from N/P 3 to N/P 5 the box width was enlarged, which indicated a high polydispersity with respect to the number of encapsulated mRNAs. In contrast, the density of the peptides followed different behavior compared to that of the mRNA molecules. At N/P 1, the number of R9 localizations per polyplex was very low and similar to that of a single peptide. Considering the labeling density (about 1.25% of labeled peptides were mixed with 98.75% unlabeled ones), this is compatible with individual mRNA molecules with about 100 peptides attached, an insufficient number to compact the oligonucleotides into a polyplex. At N/P 3, the number of R9 localizations slightly increased, but it was not until N/P 5 that the number abruptly grew and remained stable for higher ratios. At N/P 5 and N/P 7, the box widths were similar and again larger than that at N/P 3. The median number of simulated localizations matched the experimental data, demonstrating the validity of our model. The number of peptides for which the simulated number of localizations best matched the experimental data was about 25−30 labeled peptides per polyplexes; considering that 1.25% of the peptides were labeled, we can estimate approximately 2000−2400 peptides per polyplex. Still, for N/P 5 and 7 the box plot was broader. The simulated data always corresponded to the lower range of the plots. The frequency histograms of the number of localizations in Supporting Information Figures S9−S11 show the presence of
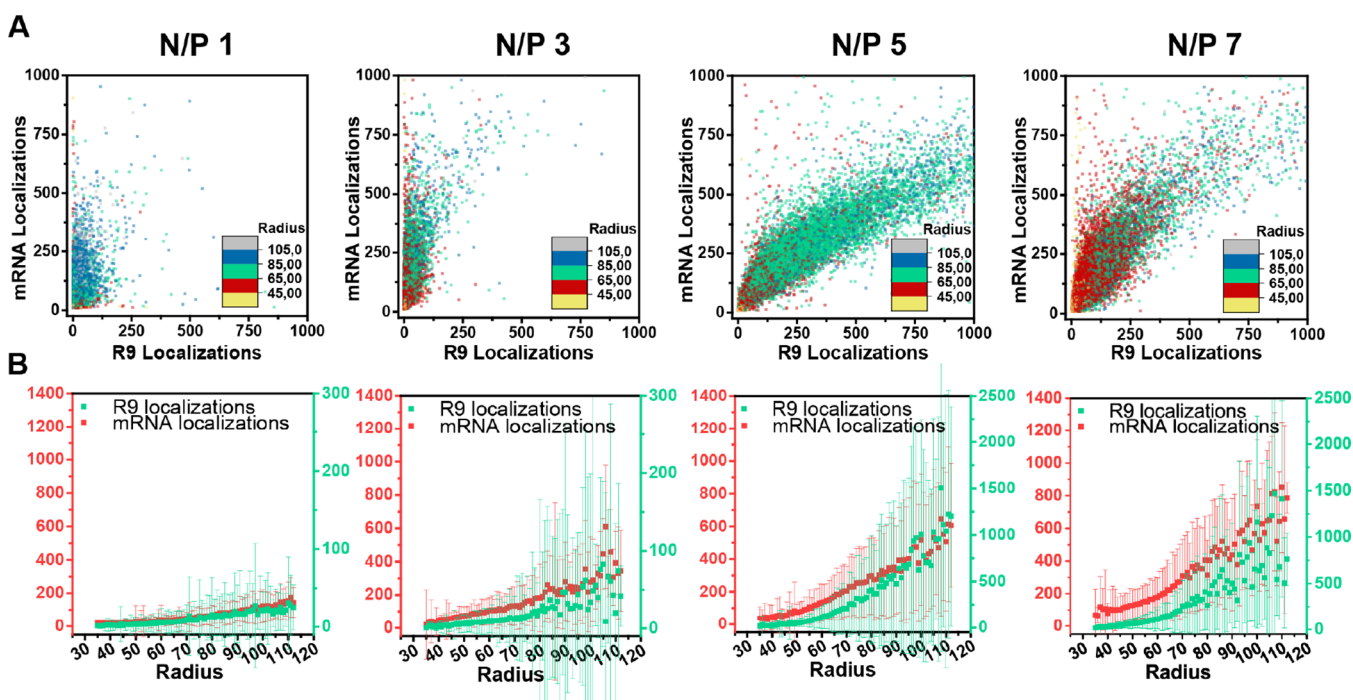
Figure 3. Correlation between the number of mRNA localizations and R9 localizations. (A) Scatter plots of the number of mRNA localizations versus the number of R9 localizations, together with a color code representing the size for each polyplex. (B) Number of localizations plotted as a function of polyplex size.

a major population in the experimental sample, which fits the simulated data, together with a tail of polyplexes with a larger number of molecules that cannot be fitted to the simulated data. The fact that the experimental data was always broader demonstrates heterogeneity in the samples, which the simulation did not recapitulate. Thus, the measured heterogeneity cannot be simply explained by the stochastic behavior of the dye; therefore, it can be concluded that the polyplex formulation does not consist of a single monodisperse population but rather of a mixture where polyplexes of different sizes and RNA quantities coexist.

To summarize these data in a molecular picture, R9 binds mRNA at N/P 1, but only from N/P 3 is this binding sufficient to condense the mRNA into polyplexes. Polyplexes from N/P 3 to N/P 7 are similar in size and amount of mRNA but change significantly with respect to the amount of peptide present in the particles. Moreover, a significant heterogeneity of the molecular composition is present, especially at N/P 5 and 7. Notably, the differences between the last three conditions and the heterogeneity in the samples would have been difficult or impossible to measure with other methods, showing the potential of dSTORM to complement existing technique for polyplex characterization.

Above, the median number of localizations per component and condition was analyzed to determine the approximate number of molecules per polyplex and the polydispersity of the samples. However, dual-color dSTORM simultaneously provides information regarding the number of localizations for each component and the size for each individual polyplex. Figure 3A,B shows a correlative analysis of these three variables. The scatter plots in Figure 3A represents the data from over 15 000 polyplexes: every dot in the chart represents one polyplex that is positioned in the graph depending on its amount of R9 or mRNA localizations. Moreover, every point is plotted in a different color depending on the size of the polyplex. With this

representation, we can draw conclusions about the relationship between the size and amount of the two components on a single-particle basis and thus with respect to the heterogeneity of the sample. At N/P 1, the mRNA localization is rather monodisperse compared to that of other samples, corresponding to the presence of single mRNA molecules. At N/P 3, the number of mRNA localizations significantly increased as did the polydispersity of the mRNA content, indicating the existence of polyplexes with multiple RNA molecules. Moreover, a correlation between the amounts of R9 and mRNA is present. This is even more evident for N/P ratios 5 and 7, where the number of R9 localizations increased overall. In particular, the polyplexes with higher mRNA localizations are the ones that show a pronounced increase in the number of R9 localizations. Following this pattern, at N/P 5 the polyplexes with high mRNA localizations display an increase in the R9 localizations, and at N/P 7, a similar correlation was observed, suggesting that the charges were saturated at N/P 5. These results prove a clear correlation in the number of molecules of each component inside individual polyplexes.

Moreover, the color code provides information on the interplay between composition and size. In all of he N/P studied, higher amounts of mRNA and R9 were found in larger polyplexes (green-blue color). The plots in Figure 3B, where the RNA and R9 content are plotted against size, also confirm this. However, the data also indicate that the density of the packing inside the polyplexes must be heterogeneous. Within the size category of a 65−85 nm radius, polyplexes differ in volume by a factor of maximally 2.2 while the number of localization varies by up to a factor of 8. Similarly, with increasing N/P more localizations for both mRNA and peptide are found for polyplexes of the same size.

Moreover, we calculated the ratio of R9 localizations per mRNA localizations and found that it was constant for N/P 1 and 3 but slightly increased with higher radii at N/P 5 and 7
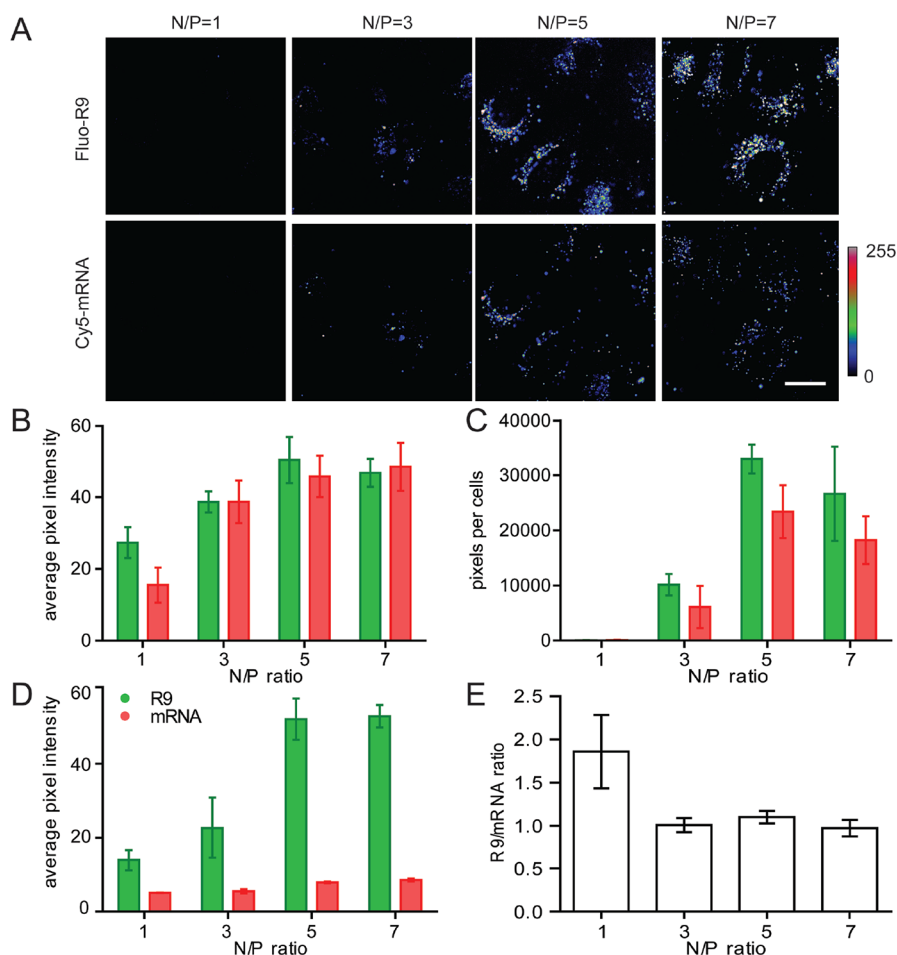
Figure 4. Dependence of cellular nanoparticle uptake on the N/P ratio. HeLa cells were incubated for 1 h with polyplexes consisting of Cy5-mRNA and fluorescein-labeled R9 at the indicated N/P ratios, followed by washing and confocal microscopy of living cells. Labeled peptide was mixed with unlabeled peptide in a ratio of 1:10. The mRNA concentration was constant at 4.5 pM for all N/P ratios, corresponding to peptide concentrations of 0.5, 1.5, 2.5, and 3.5 μM for N/P 1, 3, 5 and 7, respectively. (A) Cellular uptake and intracellular distribution. To facilitate the discrimination of intensities, a false color look-up table has been employed. The scale bar corresponds to 20 μm. (B) Average pixel intensities for vesicular fluorescence. (C) Pixels per cell as a measure of the number and size of endocytic vesicles. (D) Average pixel intensity for fluorescence outside cells, recorded at a higher detector gain. (E) Ratio of peptide over mRNA fluorescence intensity. Ratios were calculated for the vesicular intensities of each analysis image and averaged. Error bars correspond to the standard deviation for normalized data of two independent experiments.

(Supporting Information Figure S13). These results indicate that the density of polyplexes prepared at the same N/P is overall similar, although there is a trend of higher ratios at higher radii.

Importantly, the estimated number of about 2000 peptides per polyplex is fully consistent with the increase in mRNA localizations by about a factor of 3 when going from a single mRNA molecule to a polyplex. Two thousand peptides correspond to 18 000 positive charges, which, at an N/P ratio of 3, can accommodate 6000 negative charges. Because the mRNA is 1929 nucleotides in length, about 3 mRNA molecules carry this charge.

Altogether our measurements depict some important structural aspects of polyplexes: (i) a significant heterogeneity is present, with polyplexes varying significantly in size and composition; (ii) a correlation between the two components is present, with more R9 necessary to pack a higher copy number of mRNA inside the same polyplex; and (iii) higher mRNA content results in larger sizes.

Next, we aimed to assess whether the STORM analyses could lead to a better understanding of cell biological experiments. For this purpose, polyplexes were formed with Cy5-mRNA and fluorescein-labeled R9. We had shown before that fluorescein and Alexa488-labeled R9 yield equivalent results.[36] In this case, fluorescein-labeled R9 was mixed with unlabeled peptide in a ratio of 1:10. As confirmed by DLS, polyplexes with diameters ranging from 70 to 130 nm were formed for all N/P ratios. HeLa cells were incubated with polyplexes at constant concentrations of mRNA, resulting in increasing concentrations of peptide. These concentrations were proved to be noncytotoxic for cells at any of the N/P ratios (Supporting Information Figure S14). Then, intracellular fluorescence was recorded by confocal microscopy after 1 h of incubation (Figure 4A). For N/P 1, corresponding to a concentration of fluorescein-labeled peptide of 0.05 μM, hardly any cell-associated fluorescence could be detected. From N/P 3, vesicular fluorescence was presented that further increased to an N/P ratio of 5 with no further increase to N/P 7 (Figure 4A). Quantitative image analysis demonstrated that both the mean intensity of vesicular fluorescence (Figure 4B) and the total number of vesicular pixels per cell as a measure of the number of endosomes increased from N/P 1 to N/P 5 (Figure 4C). At N/P 1, almost no polyplex was internalized, and at N/P 3, the amount increased, as it also did at N/P 5 and 7. These data demonstrate that at N/P 5 the polyplexes had the right composition to be internalized.
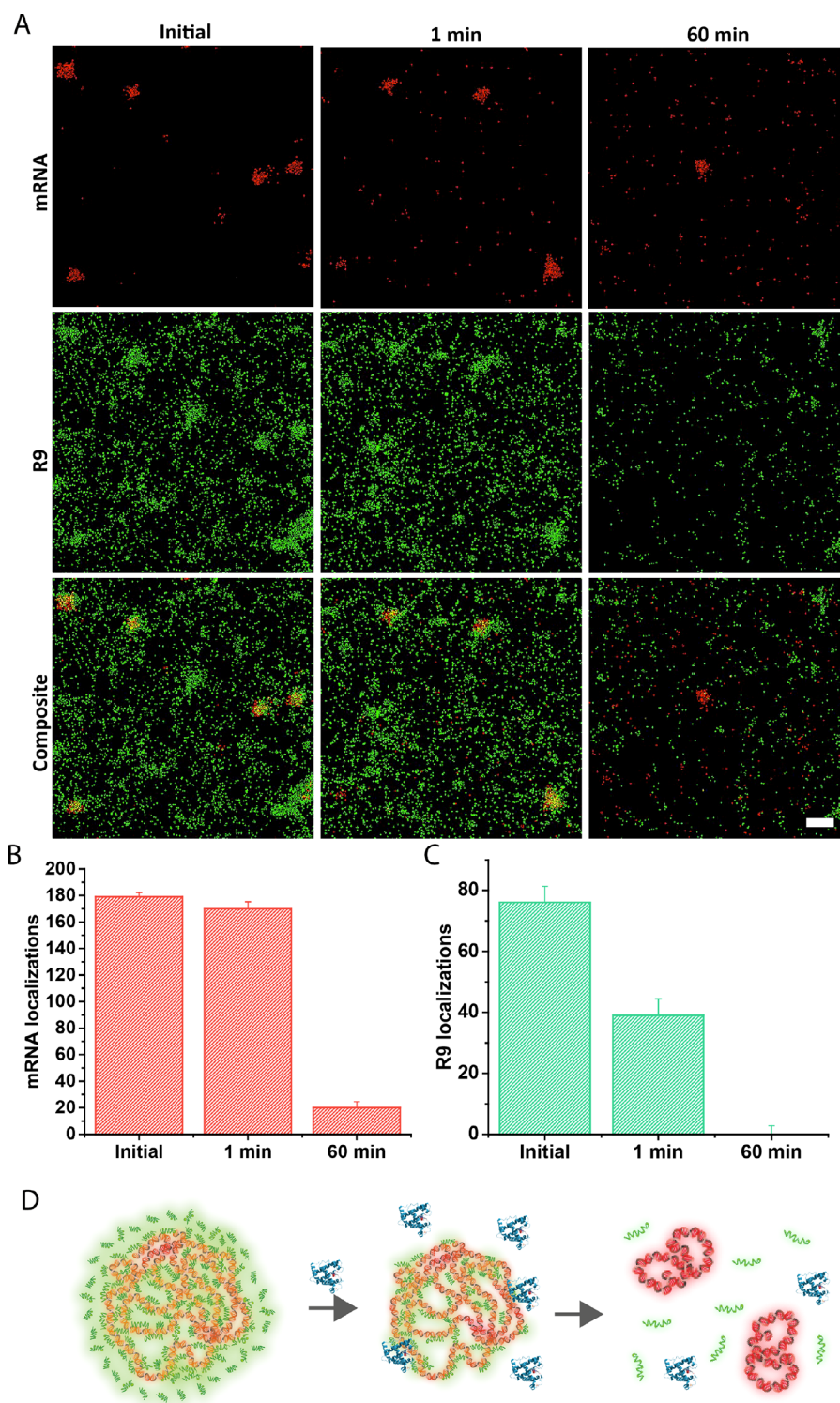
Figure 5. Stability of polyplexes in serum. (A) dSTORM image of the N/P 5 polyplexes initially and after being incubated with 20% FBS for 1 min and 1 h. Scale bar 200 nm. (B) Number of mRNA localizations of N/P 5 polyplexes after being incubated with 20% FBS for 1 min and 1 h. (C) Number of R9 localizations of N/P 5 polyplexes after being incubated with 20% FBS for 1 min and 1 h. (D) Schematic representation of the destabilization of the polyplexes in time in the presence of serum.

Even though the cells were washed in order to reduce extracellular out-of-focus fluorescence, there was still some fluorescence left. For the peptide, this extracellular fluorescence strongly increased with increasing N/P ratio, consistent with the STORM results that had demonstrated the incomplete incorporation of peptide from N/P ratios larger than 3 (Figure

4D). Moreover, we divided both mean fluorescence intensities (peptide vs mRNA) to assess the ratio of peptide per mRNA in the internalized poyplexes (Figure 4E). Interestingly, from N/P 3 to 7 this value remained constant. This observation proves that a specific composition of the polyplexes is needed to be internalized by the cells. From our STORM data, we

demonstrated that at N/P 3 most of the polyplexes did not have enough peptide incorporated to pack the mRNA; therefore, we hypothesize that only a small population of polyplexes at N/P 3 have the right composition, which corresponds to the lower internalization observed. Finally, the higher ratio at N/P 1 is consistent with the absence of polyplex formation so that only free peptide was internalized.

Having established the methodology to measure the polyplex size and composition, we exploited the ability of dSTORM to perform analyses in complex media such as blood serum. Polyplexes are designed to be intravenously injected into the bloodstream, being in contact with proteins and other biomolecules that can destabilize the complex. Therefore, it is of major importance to understand the stability of the polyplexes in serum. Classically, gel retardation assays are used to assess the release and decomposition of polyplexes.[7] Using dSTORM imaging, we expected to obtain information on the mechanism of decomplexation because we were able to track the composition and size of polyplexes. To this end, we incubated polyplexes at 37 °C with fetal bovine serum (FBS) at concentrations of 1, 20, and 100% for 1 min and 1 h followed by deposition on coverslips. Then, dSTORM images of the complexes were acquired (Figure 5 and Supporting Information Figure S15). The behavior of the polyplexes was similar when incubated with 1 or 20% FBS. Under these conditions, after 1 min the mRNA content in the polyplexes remained stable compared to the initial composition, indicating that the polyplexes were not releasing their payload. However, we observed a decrease in the number of peptide molecules. After 1 min of serum incubation, only half of the initial peptide localizations were detected. In contrast, after 1 h of FBS incubation both the numbers of mRNA and R9 molecules abruptly dropped (Figure 5A−C). Altogether, these results indicate that the serum proteins interact with the polyplexes in two stages as schematically represented in Figure 5D: (i) serum rapidly removes peptides from the polyplexes without compromising the mRNA compacted inside the particle (minute timescale) and (ii) proteins destabilize the complexes causing the release of mRNA molecules (hour timescale). We envision that the ability of dSTORM to provide additional information about the mechanism of polyplex disassembly will support the study and design of gene carriers with improved serum stability.

We presented an in-depth study of the structure and composition of polyplexes containing mRNA and cell-penetrating peptide R9 using dSTORM imaging. Our results show both qualitative and quantitative differences in the mRNA and peptide content of individual polyplexes formed at different N/P ratios. Importantly, a minimum excess of peptide was required to condense the mRNA into polyplexes because at N/P 1 no distinct clusters could be observed. At N/P 3, the number of peptides was sufficient to pack the mRNA into compact polyplexes. With an increase in N/P, the R9 content and peptide to mRNA ratio in the polyplexes further increased, reaching a plateau at around N/P 5. The possibility to image individual polyplexes allowed us to dissect the relationship between the relative content of the two components and the size of the polyplexes, demonstrating a next-to-positive correlation of both components with respect to size, some heterogeneity in the packing density, and an increase in the packing density with increasing N/P ratio. Our analyses clearly demonstrate that the insights gained through the STORM analysis of the polyplexes directly translate into a better understanding of cellular uptake

experiments. From N/P 5 to 7, the characteristics of the polyplexes are the same, which explains why they have the same cellular uptake efficiency. At N/P 3, sufficient mRNA encapsulation had been achieved for only a fraction of the polyplexes as evident from the large heterogeneity of polyplexes at the molecular level, demonstrated by STORM. Finally, the imaging of the destabilization of polyplexes in the presence of serum provided mechanistic insights into the disassembly mechanism, a crucial aspect for the in vivo performance of gene carriers. Our study highlights the potential of multicolor super-resolution microscopy to shed new light on the nanoscale structure and stoichiometry of polyplexes, a key aspect for the understanding of gene delivery carriers. Future perspectives include a study of structure−activity relationships for a variety of polymeric, lipidic, and peptidic carriers and a study of the structure of polyplexes in cells after internalization. In this framework it has to be considered that STORM imaging is possible only in fixed cells and therefore optimization of the fixation procedure to retain the polyplex structure is necessary. In conclusion, we believe that super-resolution microscopy can nicely complement the current techniques for polyplex characterization contributing to the guidance of the design of more effective oligonucleotide therapeutics.

ASSOCIATED CONTENT

Ⓢ Supporting Information

The Supporting Information is available free of charge on the ACS Publications website at DOI: 10.1021/acs.nanolett.8b04407.

> Materials and methods, a detailed explanation of the simulations used, and additional experimental results (PDF)

AUTHOR INFORMATION

Corresponding Authors
*E-mail: Roland.Brock@radboudumc.nl.
*E-mail: l.albertazzi@tue.nl.

ORCID Ⓘ
Roland Brock: 0000-0003-1395-6127
Lorenzo Albertazzi: 0000-0002-6837-0812

Author Contributions
⊥These authors contributed equally.

Notes
The authors declare no competing financial interest.

ACKNOWLEDGMENTS

ABBREVIATIONS

dSTORM, direct stochastic optical reconstruction microscopy; CPP, cell-penetrating peptide; DLS, dynamic light scattering; R9, L-nona-arginine; FBS, fetal bovine serum

■ REFERENCES

(1) Koren, E.; Torchilin, V. P. *Trends Mol. Med.* **2012**, *18* (7), 385−393.

(2) Collado Camps, E.; Brock, R. *Bioorg. Med. Chem.* **2018**, *26* (10), 2780−2787.

(3) Heitz, F.; Morris May, C.; Divita, G. *Br. J. Pharmacol.* **2009**, *157* (2), 195−206.

(4) Lee, S. H.; Castagner, B.; Leroux, J.-C. *Eur. J. Pharm. Biopharm.* **2013**, *85* (1), 5−11.

(5) Zhang, P.; Wagner, E. *Top. Curr. Chem.* **2017**, *375* (2), 26.

(6) Lächelt, U.; Wagner, E. *Chem. Rev.* **2015**, *115* (19), 11043−11078.

(7) Scomparin, A.; Polyak, D.; Krivitsky, A.; Satchi-Fainaro, R. *Biotechnol. Adv.* **2015**, *33* (6, Part 3), 1294−1309.

(8) Debus, H.; Baumhof, P.; Probst, J.; Kissel, T. *J. Controlled Release* **2010**, *148* (3), 334−343.

(9) Meng, Z.; O'Keeffe-Ahern, J.; Lyu, J.; Pierucci, L.; Zhou, D.; Wang, W. *Biomater. Sci.* **2017**, *5* (12), 2381−2392.

(10) Sahin, U.; Karikó, K.; Türeci, Ö. *Nat. Rev. Drug Discovery* **2014**, *13* (10), 759−780.

(11) van Asbeck, A. H.; Beyerle, A.; McNeill, H.; Bovee-Geurts, P. H. M.; Lindberg, S.; Verdurmen, W. P. R.; Hällbrink, M.; Langel, Ü.; Heidenreich, O.; Brock, R. *ACS Nano* **2013**, *7* (5), 3797−3807.

(12) Lee, J. B.; Hong, J.; Bonner, D. K.; Poon, Z.; Hammond, P. T. *Nat. Mater.* **2012**, *11* (4), 316−322.

(13) Patil, M. L.; Zhang, M.; Taratula, O.; Garbuzenko, O. B.; He, H.; Minko, T. *Biomacromolecules* **2009**, *10* (2), 258−266.

(14) Ofek, P.; Fischer, W.; Calderón, M.; Haag, R.; Satchi-Fainaro, R. *FASEB J.* **2010**, *24* (9), 3122−3134.

(15) García-Sosa, A. T.; Tulp, I.; Langel, K.; Langel, Ü. *BioMed Res. Int.* **2014**, *2014*, 257040.

(16) Meneksedag-Erol, D.; Tang, T.; Uludağ, H. *Biomaterials* **2014**, *35* (25), 7068−7076.

(17) Majzoub, R. N.; Ewert, K. K.; Safinya, C. R. *Philos. Trans. R. Soc., A* **2016**, *374* (2072), 20150129.

(18) van der Zwaag, D.; Vanparijs, N.; Wijnands, S.; De Rycke, R.; De Geest, B. G.; Albertazzi, L. *ACS Appl. Mater. Interfaces* **2016**, *8* (10), 6391−6399.

(19) Duro-Castano, A.; Nebot Vicent, J.; Niño-Pariente, A.; Armiñán, A.; Arroyo-Crespo, J.; Paul, A.; Feiner-Gracia, N.; Albertazzi, L.; Vicent, M. *Adv. Mater.* **2017**, *29* (39), 1702888.

(20) Ardizzone, A.; Kurhuzenkau, S.; Illa-Tuset, S.; Faraudo, J.; Bondar, M.; Hagan, D.; Van Stryland, E. W.; Painelli, A.; Sissa, C.; Feiner, N.; et al. *Small* **2018**, *14*, 1703851.

(21) Burgert, A.; Schlegel, J.; Bécam, J.; Doose, S.; Bieberich, E.; Schubert-Unkmeir, A.; Sauer, M. *Angew. Chem.* **2017**, *129* (22), 6227−6231.

(22) Letschert, S.; Göhler, A.; Franke, C.; Bertleff-Zieschang, N.; Memmel, E.; Doose, S.; Seibel, J.; Sauer, M. *Angew. Chem., Int. Ed.* **2014**, *53* (41), 10921−10924.

(23) Fricke, F.; Beaudouin, J.; Eils, R.; Heilemann, M. *Sci. Rep.* **2015**, *5*, 14072.

(24) Zanacchi, F. C.; Manzo, C.; Alvarez, A. S.; Derr, N. D.; Garcia-Parajo, M. F.; Lakadamyali, M. *Nat. Methods* **2017**, *14* (8), 789−792.

(25) Puchner, E. M.; Walter, J. M.; Kasper, R.; Huang, B.; Lim, W. A. *Proc. Natl. Acad. Sci. U. S. A.* **2013**, *110* (40), 16015−16020.

(26) Ezzat, K.; EL Andaloussi, S.; Zaghloul, E. M.; Lehto, T.; Lindberg, S.; Moreno, P. M. D.; Viola, J. R.; Magdy, T.; Abdo, R.; Guterstam, P.; et al. *Nucleic Acids Res.* **2011**, *39* (12), 5284−5298.

(27) Wu, R. P.; Youngblood, D. S.; Hassinger, J. N.; Lovejoy, C. E.; Nelson, M. H.; Iversen, P. L.; Moulton, H. M. *Nucleic Acids Res.* **2007**, *35* (15), 5182−5191.

(28) Futaki, S.; Ohashi, W.; Suzuki, T.; Niwa, M.; Tanaka, S.; Ueda, K.; Harashima, H.; Sugiura, Y. *Bioconjugate Chem.* **2001**, *12* (6), 1005−1011.

(29) Vaidyanathan, S.; Chen, J.; Orr, B. G.; Banaszak Holl, M. M. *Mol. Pharmaceutics* **2016**, *13* (6), 1967−1978.

(30) Lehto, T.; Vasconcelos, L.; Margus, H.; Figueroa, R.; Pooga, M.; Hällbrink, M.; Langel, Ü. *Bioconjugate Chem.* **2017**, *28* (3), 782−792.

(31) Jekhmane, S.; de Haas, R.; Paulino da Silva Filho, O.; van Asbeck, A. H.; Favretto, M. E.; Hernandez Garcia, A.; Brock, R.; de Vries, R. *Nucleic Acid Ther.* **2017**, *27* (3), 159−167.

(32) Zhuang, X. *Nat. Photonics* **2009**, *3* (7), 365−367.

(33) Coltharp, C.; Yang, X.; Xiao, J. *Curr. Opin. Struct. Biol.* **2014**, *28*, 112−121.

(34) Feiner-Gracia, N.; Beck, M.; Pujals, S.; Tosi, S.; Mandal, T.; Buske, C.; Linden, M.; Albertazzi, L. *Small* **2017**, *13* (41), 1701631.

(35) Albertazzi, L.; van der Zwaag, D.; Leenders, C. M. A.; Fitzner, R.; van der Hofstad, R. W.; Meijer, E. W. *Science* **2014**, *344* (6183), 491−495.

(36) Wallbrecher, R.; Ackels, T.; Olea, R. A.; Klein, M. J.; Caillon, L.; Schiller, J.; Bovée-Geurts, P. H.; van Kuppevelt, T. H.; Ulrich, A. S.; Spehr, M.; et al. *J. Controlled Release* **2017**, *256*, 68−78.